

# High sensitivity of $^{17}\text{O}$ NMR to p-d hybridization in transition metal perovskites: first principles calculations of large anisotropic chemical shielding

Daniel L. Pechkis, Eric J. Walter and Henry Krakauer

*Department of Physics, College of William and Mary, Williamsburg, VA 23187-8795.*

(Dated: November 22, 2018)

A first principles embedded cluster approach is used to calculate O chemical shielding tensors,  $\hat{\sigma}$ , in prototypical transition metal oxide  $\text{ABO}_3$  perovskite crystals. Our principal findings are 1) a large anisotropy of  $\hat{\sigma}$  between deshielded  $\sigma_x \simeq \sigma_y$  and shielded  $\sigma_z$  components ( $z$  along the Ti-O bond); 2) a nearly linear variation, across all the systems studied, of the isotropic  $\sigma_{\text{iso}}$  and uniaxial  $\sigma_{\text{ax}}$  components, as a function of the B-O-B bond asymmetry. We show that the anisotropy and linear variation arise from large paramagnetic contributions to  $\sigma_x$  and  $\sigma_y$  due to virtual transitions between O(2p) and unoccupied B( $nd$ ) states. The calculated isotropic  $\delta_{\text{iso}}$  and uniaxial  $\delta_{\text{ax}}$  chemical shifts are in good agreement with recent  $\text{BaTiO}_3$  and  $\text{SrTiO}_3$  single crystal  $^{17}\text{O}$  NMR measurements. In  $\text{PbTiO}_3$  and  $\text{PbZrO}_3$ , calculated  $\delta_{\text{iso}}$  are also in good agreement with NMR powder spectrum measurements. In  $\text{PbZrO}_3$ ,  $\delta_{\text{iso}}$  calculations of the five chemically distinct sites indicate a correction of the experimental assignments. The strong dependence of  $\hat{\sigma}$  on covalent O(2p)-B( $nd$ ) interactions seen in our calculations indicates that  $^{17}\text{O}$  NMR spectroscopy, coupled with first principles calculations, can be an especially useful tool to study the local structure in complex perovskite alloys.

PACS numbers: 71.15.-m, 76.60.Cq, 77.84.-s, 31.15.Ar

Keywords: Chemical shielding, first principles, NMR, gaussian atomic basis, GTO basis

## I. INTRODUCTION

Due to their reversible polarization and strong electro-mechanical coupling, ferroelectric perovskite oxides are key components in many electronic and mechanical devices such as sensors, actuators, and random access memory.<sup>1</sup> The largest piezoelectric response occurs when competing structural instabilities are present,<sup>2</sup> so that the local structure depends sensitively on strain, external fields, and chemical composition, as for example, near the morphotropic phase boundary near  $x = 1/2$  in  $\text{Pb}(\text{Zr}_{1-x}\text{Ti}_x)\text{O}_3$  (PZT). Nuclear magnetic resonance (NMR) can be an important probe of local structure, and NMR has increasingly been used to study complex ferroelectric alloys.<sup>3,4,5</sup> First-principles calculations of NMR properities are likely to play an important role in helping to interpret complex measured spectra.

A material's characteristic NMR spectra is determined by the coupling of the nuclear magnetic dipole and electric quadrupole moments with the local magnetic field and with the electric field gradients (EFG), respectively.<sup>6</sup> The chemical shielding tensor,  $\hat{\sigma}$ , determines the local magnetic field at a nucleus

$$\mathbf{B} = (1 - \hat{\sigma})\mathbf{B}_{\text{ext}}, \quad (1)$$

where the induced field  $\mathbf{B}_{\text{ind}} = -\hat{\sigma}\mathbf{B}_{\text{ext}}$  arises from electronic screening currents. Theoretical determination of the chemical shielding tensor,  $\hat{\sigma}$ , is more subtle than the EFGs, since the latter depend only on the ground state charge density. Linear response methods have long been used to calculate  $\hat{\sigma}$  for isolated molecules and clusters.<sup>7,8,9,10,11,12,13</sup> In extended systems complications arise due to the use of periodic boundary conditions

(PBC),<sup>14,15,16</sup> and implementations have been limited to planewave-based methods. Recently, an alternative to the linear response method has been proposed based on calculations of the orbital magnetization.<sup>17,18,19,20</sup> If this approach proves successful, calculations of  $\hat{\sigma}$  could be implemented in other standard band structure codes, including all-electron methods.<sup>19</sup>

Calculations of  $\hat{\sigma}$  in crystals and extended systems have largely used finite-size clusters, due to the lack of generally available PBC computer codes with NMR functionality. Accurate results can be obtained with this approach if the screening currents are sufficiently localized near the target nucleus, and if its local environment is adequately modeled by the cluster. Embedded cluster techniques have been successfully used in crystals and macromolecules to obtain nuclear quadrupole resonance spectrum, ligand to metal charge transfer excitations, photoemission, electric field gradients, and hyperfine coupling in high  $T_c$  superconductors.<sup>21,22,23,24</sup>

Such calculations have generally used standard all-electron quantum chemistry methods, which are widely available in many quantum chemistry computer programs, such as GAUSSIAN.<sup>25,26</sup> These methods are very mature and can calculate  $\hat{\sigma}$  with a range of approximations, using well tested Gaussian type orbital (GTO) basis sets.<sup>27</sup> In increasing order of computational cost, these methods range from mean-field type [density functional theory (DFT), Hartree Fock (HF), and hybrid methods] to correlated approximations [such as second-order Moller-Plesset (MP2) perturbation and coupled cluster (CC) methods].<sup>7,28,29</sup> The present cluster calculations exploit this flexibility to calculate chemical shieldings, comparing DFT/GGA, restricted HF (RHF), and hybrid-DFT/B3LYP calculations. Currently, only LDA

and GGA DFT approximations are available for NMR calculations in PBC methods.

For covalently bonded systems, cluster calculations typically use hydrogen atoms to terminate dangling bonds at the cluster surface.<sup>8</sup> Instead, we use point charge embedding<sup>30</sup> to model the long range Coulomb interactions in the  $\text{ABO}_3$  materials studied here. Additional techniques are also used to better handle the polarizable character of the large  $\text{O}^{2-}$  anion and also to control surface depolarization effects.

In this paper, we show that the embedded cluster approach can yield accurate oxygen  $\hat{\sigma}$  for transition metal perovskites. The focus is on four prototypical materials:  $\text{BaTiO}_3$ ,  $\text{SrTiO}_3$ ,  $\text{PbTiO}_3$  and  $\text{PbZrO}_3$ . Strong covalency between the O and transition metal B atoms (and between the A and O atoms in Pb based materials) delicately balance ionic electrostatic interactions in these materials and related alloys, resulting in a wide variety of interesting and technologically important properties. The classic ferroelectric material  $\text{BaTiO}_3$  exhibits three reversible temperature dependent ferroelectric phases.  $\text{SrTiO}_3$  is a key constituent in superlattice structures with novel material properties.<sup>2</sup>  $\text{PbTiO}_3$  is the prototypical Pb based ferroelectric. The strong covalency of Pb on the A-site is responsible for the large  $c/a = 1.065$  ratio in  $\text{PbTiO}_3$ , and it plays a similar role in large electromechanical response of relaxor ferroelectrics such as PMN.<sup>31</sup>  $\text{PbZrO}_3$  adopts a complicated non-polar antiferrodistortive structure with five chemically inequivalent O sites, which our calculations reproduce.  $\text{PbZrO}_3$  is also of the end-point compounds, together with  $\text{PbTiO}_3$ , of the PZT solid solution series.

The paper is organized as follows. The theoretical approach is described in Sec. II. Calculated results for  $\text{ABO}_3$  systems are presented in Sec. III, and an analysis of the results is presented in Sec. IV. Finally, we summarize and conclude in Sec. V.

## II. THEORETICAL APPROACH

After briefly reviewing  $\hat{\sigma}$  conventions, the construction of embedded clusters for ionic materials is described. Finally, we describe the quantum chemistry methods and GTO basis sets used in the calculations.

### A. Chemical shielding tensor

The chemical shielding tensor  $\hat{\sigma}$  [Eq. (1)] is a mixed second derivative of the ground state energy with respect to the applied magnetic field and nuclear magnetic moment.<sup>7</sup> As such, it is an asymmetric second rank tensor with nine independent components in general, although its symmetry can be higher, depending on the site symmetry of the target nucleus.<sup>32</sup> The anti-symmetric part of  $\hat{\sigma}$  contributes negligibly to the NMR resonance frequency shift, since it enters only in second order,<sup>33,34</sup> although it

can contribute to relaxation.<sup>35</sup> The symmetric part can always be diagonalized, and the NMR frequency is determined by the following combinations of its principal axis components<sup>36</sup>

$$\begin{aligned}\sigma_{\text{iso}} &= \frac{1}{3}(\sigma_x + \sigma_y + \sigma_z) = \frac{1}{3}\text{Tr } \hat{\sigma} \\ \sigma_{\text{ax}} &= \frac{1}{6}(2\sigma_z - \sigma_x - \sigma_y) = \frac{1}{2}(\sigma_z - \sigma_{\text{iso}}) \\ \sigma_{\text{aniso}} &= \frac{1}{2}(\sigma_y - \sigma_x),\end{aligned}\quad (2)$$

where  $\sigma_{\text{iso}}$ ,  $\sigma_{\text{ax}}$ , and  $\sigma_{\text{aniso}}$  are the isotropic, uniaxial, and anisotropic components, respectively. In this paper,  $\sigma_z$  is chosen to correspond to the principal axis that is mostly nearly along the B-O-B bond direction.

Positive values of  $\sigma$  are conventionally denoted as shielding the external field, while negative elements are referred to as deshielding [see Eq. (1)]. Measurements of  $\hat{\sigma}$  are usually reported with respect to a reference compound, where the chemical shift tensor is defined as<sup>28</sup>

$$\hat{\delta} = -(\hat{\sigma} - \sigma_{\text{iso}}^{\text{ref}}).\quad (3)$$

### B. Embedded clusters

An embedded cluster model is depicted in Fig. 1. Its core consists of real, or “quantum” (QM) atoms, with the target O atom at its center. The total number of electrons is determined by satisfying the nominal formal valence of all the QM atoms. The  $\text{A}_4\text{B}_2\text{O}_{15}$  QM cluster in the figure thus has a net charge of -14. The QM cluster is embedded in the classical potential due to point charges, pseudopotentials, and, in some cases, an external electric field to cancel surface depolarization effects, as described in following subsections. The atomic site designations nn and nnn, used below, denote nearest-neighbor and next-nearest-neighbor sites, respectively, and are based on the ideal structures. Thus, for example, the Ti atom in tetragonal  $\text{P4mm}$   $\text{PbTiO}_3$  would be regarded as having six nn O atoms, despite the distortion of the  $\text{TiO}_6$  octahedron. In the actual calculations, the tetragonal distortion results in two chemically inequivalent  $\text{O}_{\text{eq}}$  and  $\text{O}_{\text{ax}}$  atoms ( $\text{O}_{\text{ax}}$  lying on the polar axis), which require two separate embedded cluster calculations.

#### 1. Quantum cluster

In all the QM clusters considered in this paper, the target oxygen atom is fully coordinated with QM atoms located at its nn and nnn sites. Secondly, the target atom’s nn QM atoms are themselves fully coordinated with nn QM atoms. Finally additional QM atoms are added, as required by ideal perovskite symmetry. This procedure results in a 21 QM-atom cluster:  $(\text{A}_4\text{B}_2\text{O}_{15})^{14-}$ , depicted in Fig. 1, where A = Sr, Ba, or Pb; B = Ti or Zr. This includes two corner-shared  $\text{BO}_6$  octahedra, centered on the targeted O atom (11 O and 2 B atoms), the target atom’s 4 nnn A cations, and 4 additional O atoms, which

are also one lattice constant away from the center atom. Tests with larger QM clusters were used to estimate convergence of the chemical shielding tensor with respect to cluster size, as discussed in Sec. II C.

### 2. Madelung potential: point charges

Next, the QM cluster is embedded in the crystal environment by surrounding it with a large array of point charges. The purpose of the point charges is to better simulate the crystal environment by generating the correct crystalline electrostatic Madelung potential in the QM region. The correct Madelung potential also plays a key role in stabilizing the  $O^{2-}$  ion, as has been shown in Gordon-Kim<sup>37</sup> type models,<sup>38,39</sup> where the internal energy of ionic systems is determined from the energy of overlapping ionic charge densities. The finite point charge distribution is determined using the EWALD program,<sup>30</sup> as follows. In a first step, EWALD calculates the Madelung potential with the Ewald method for PBC, using nominal ionic values (*e.g.*,  $\tilde{Q}_i = -2$  and  $\tilde{Q}_i = +2$  for  $O^{2-}$  and  $Pb^{2+}$ , respectively) for the atoms placed at crystallographic positions of the targeted system. In a second step, EWALD retains the nearest  $\mathcal{O}(10^4)$   $\tilde{Q}_i$  centered on the target atom, adjusting the values of the outermost  $\tilde{Q}_i$  to reproduce the Madelung electrostatic potential on and in the vicinity of the QM atoms. In this second step, the nearest  $\simeq 500 - 750$   $\tilde{Q}_i$  are fixed at their nominal values, and, in addition, the net monopole and dipole moments of the point charge distribution are constrained to vanish.

### 3. Boundary compensation via empty pseudopotentials

To accelerate the convergence of  $\hat{\sigma}$  with respect to the size of the QM cluster, it is advantageous to control the artificial polarization of boundary O(2p) states. This arises from the strongly attractive electrostatic potential of neighboring cation point charges for QM oxygen atoms on the periphery of the cluster. To alleviate this, the nn and nnn cation point charges of boundary O atoms are replaced by “empty” pseudopotentials (ePSP),<sup>40</sup> as illustrated in Fig. 1. The ePSP is defined as follows: i) it is a large core pseudopotential for the most loosely bound valence electrons of the corresponding cation (*e.g.*, a  $Ti^{4+}$  PSP); ii) there are no GTO basis functions associated with this site. The resulting modified cation classical potential simulates the Pauli cation core repulsion, thereby reducing the artificial polarization of boundary O(2p) states.<sup>40</sup> In the embedded 21 atom QM cluster discussed above, for example, 26 boundary point charges are replaced by ePSPs (labeled as  $A^*$  or  $B^*$ ), yielding a  $(A_4B_2O_{15})^{14-} - A_{16}^*B_{10}^*$  cluster, which is surrounded by the remaining  $\simeq \mathcal{O}(10^4)$  point charges.

### 4. Cancellation of electric depolarization fields

Due to the spontaneous electric polarization found in some materials, such as tetragonal  $PbTiO_3$ , a macroscopic depolarizing electric field is present in finite samples, in the absence of surface compensating charges. Calculations using PBC are implicitly done in zero total macroscopic electric field, which automatically excludes surface depolarization effects. In the present finite size clusters, a depolarizing electric field can arise from a possible net dipole moment, due to polarization of the quantum mechanical charge density, *i.e.*, from the wave functions of the QM cluster. The net dipole moment due to the point charges and ePSPs is zero by construction, as discussed above. The resulting depolarizing electric field is removed in the calculation, by applying an external electric field in the opposite direction. The magnitude of the external field is chosen so that the force on the central target atom matches that of an all-electron PBC linearized augmented plane wave (LAPW)<sup>41</sup> calculation. In normal equilibrium conditions, using experimentally determined structures, the LAPW forces are usually small, since the theoretical structure is usually close to that of experiment.

### C. Computational details

The embedded cluster calculations were performed with the GAUSSIAN computational package.<sup>25,26</sup> The chemical shielding tensor was determined using the continuous set of gauge transformations (CSGT) method.<sup>42,43</sup> The gauge-independent atomic orbital (GIAO) method<sup>44</sup> was also used for comparison in some cases. The gauge origin in GIAO is at the target atom, yielding a useful decomposition into diamagnetic and paramagnetic components, as discussed further below and in the next Section. We did not include a surface dependent magnetic depolarization contribution to  $\delta_{iso}$ , which depends on the magnetic susceptibility.<sup>45,46</sup>

Calculations were done using the DFT hybrid B3LYP,<sup>47</sup> as well as the generalized gradient approximation (GGA), using the PW91 form.<sup>48</sup> The B3LYP calculations were found to yield generally better agreement with experiment (Sec. III) than GGA. Site-centered GTO basis functions were associated with all the QM atoms. All-electron treatments were used for the O and Ti atoms, while the other QM atoms were represented using scalar-relativistic small core (RSC) pseudopotentials [also called effective core potentials (ECPs)]. All basis sets and ECPs listed below were taken from the EMSL website.<sup>27</sup> O-centered  $(A_4B_2O_{15})^{14-}$  QM clusters were used in the calculations, suitably embedded with point charges and ePSPs, as discussed in Sec. II B). Test calculations for larger clusters were used to check size convergence, as discussed at the end of this section.

The RSC ECPs for the QM atoms were Sr(28), Zr(28), Ba(46), Pb (60), where the number of core electrons is

shown in parenthesis. These pseudopotentials are generally specified by the same label as their associated basis sets listed below, except where otherwise indicated. For ePSPs (Sec. II B 3), which have no associated GTOs, scalar-relativistic large core (RLC) ECPs were used as follows: CRENBS RLC for Ti(18) and Zr(36); Stuttgart RLC for Sr(36) and Ba(54). [The Ba ePSP was also used for the Pb ePSP atoms, because we could not find a large core  $\text{Pb}^{2+}$  quantum chemistry type pseudopotential in the standard databases.] The following GTO basis sets were found to give well-converged results: O(IGLO-III), Ti(cc-pwCVTZ-NR), Zr(cc-pwCVTZ-PP), and Pb(cc-pVTZ-PP). For the Sr and Ba atoms, the associated Stuttgart RSC 1997 basis sets were used. The correlation consistent basis sets were employed in this study, because this basis function series facilitates a systematic study of chemical shift convergence with respect to basis set size. (We could not find correlation consistent basis sets for Sr and Ba.) The O(IGLO-III) basis set was used, because it was specifically designed for magnetic property calculations. In convergence tests, we found that it had quadruple- $\zeta$  (QZ) accuracy even though it has fewer basis functions.

In  $\text{SrTiO}_3$ , for example, B3LYP CSGT principle value components calculated with the aforementioned basis sets differed by no more than 10 ppm from results calculated with the O(cc-pwCVQZ), Ti(cc-pwCVQZ-NR), and Sr(def2-QZVP) basis sets, while  $\delta_{\text{iso}}$  differed by only  $\simeq 8$  ppm. In  $\text{PbTiO}_3$ , changing the Pb basis set from DZ to TZ changed  $\delta_{\text{iso}}$  by less than 10 ppm, while the difference between inequivalent O sites changed by less than 4 ppm. These results are consistent with calculations for  $\text{SrTiO}_3$ , using two different gauge methods, shown in Table I, where, in the infinite basis set limit, the CSGT and GIAO values should agree. The individual B3LYP components,  $\sigma_x = \sigma_y$  and  $\sigma_z$ , are seen to differ by 3 and 26 ppm, respectively, while  $\sigma_{\text{iso}}$  differs by only 6 ppm.

Size convergence errors of about 30 ppm in the absolute value of the chemical shieldings were estimated from calculations on larger clusters, using the above basis sets. In  $\text{SrTiO}_3$ , for example, increasing the O-centered cluster size from the  $\text{Sr}_4\text{Ti}_2\text{O}_{15}$  (21 atoms) to  $\text{Sr}_4\text{Ti}_{10}\text{O}_{47}$  (61 atoms) changed the RHF, B3LYP, and PW91  $\sigma_{\text{iso}}$  by -13, -27, and -25 ppm, respectively, while individual principal values changed by less than 16, 30, and 37 ppm. These test calculations used large core Ti pseudopotentials for the additional Ti atoms.

### III. RESULTS

Calculated chemical shielding results for the prototypical perovskites  $\text{SrTiO}_3$ ,  $\text{BaTiO}_3$ ,  $\text{PbTiO}_3$  and  $\text{PbZrO}_3$  are presented and compared to  $^{17}\text{O}$  NMR single crystal and powder spectra chemical shift measurements in this section. Calculations were performed for embedded clusters corresponding to the following structural parameters. For cubic  $\text{SrTiO}_3$ , the lattice parameter of Ref. 49

was used.  $\text{BaTiO}_3$  cubic and tetragonal P4mm structures were taken from Ref. 50; rhombohedral R3m from Ref. 51. The  $\text{PbTiO}_3$  tetragonal P4mm structure was taken from Ref. 52. For  $\text{PbZrO}_3$ , which has a complicated Pbam unit cell containing eight formula units, experimental lattice parameters from neutron scattering measurements were used together with internal coordinates determined from first principles calculations.<sup>53</sup> All calculations were carried out using the embedded cluster approach described in Sec. II, using the hybrid B3LYP exchange-correlation functional. In some cases RHF and GGA/PW91 results are reported for comparison.

Table I presents our calculated results for the principal values of the symmetrized chemical shielding tensor  $\hat{\sigma}$ . (The asymmetry in the chemical shielding tensors was less than 0.5 ppm; see Sec. II A.) The principal axis frame of the target O atom is indicated by  $x, y, z$ , where the  $z$ -axis is always identified with the local B-O-B direction. This is exact in the cubic and tetragonal crystals. For lower O-site symmetry, the  $z$ -axis well approximates the quasilinear B-O-B bond in all the structures considered here.

A striking feature in Table I is the large  $\sigma_x \simeq \sigma_y$  vs.  $\sigma_z$  anisotropy of the principal values for each case, with two large negative (deshielded) principal values and one considerably smaller positive (shielded)  $\sigma_z$  principal value. The O atoms have their highest site-symmetry in the cubic crystals, resulting in an exact two-fold  $\sigma_x = \sigma_y$  degeneracy. For lower symmetry cases, the degeneracy is lifted, but the splitting remains small in most cases; the largest splitting is 65 ppm for the O1-4g site in  $\text{PbZrO}_3$ . As shown by the GIAO calculations for  $\text{SrTiO}_3$ , the anisotropy arises from the paramagnetic components. We note that the GIAO diamagnetic components in  $\text{SrTiO}_3$  differ by only  $\simeq 40 - 50$  ppm from that of the the isolated, purely diamagnetic,  $\text{O}^{2-}$  atom.

In the fake  $\text{SrTiO}_3$  calculation, where d-like ( $\ell = 2$ ) Ti-centered GTO basis functions were deliberately excluded from the calculation, the large  $x, y$  vs.  $z$  anisotropy is absent. The fake diamagnetic values are closer to the atomic  $\text{O}^{2-}$  shielding, and the paramagnetic contributions are close to isotropic. The  $x, y$  vs.  $z$  anisotropy of the calculated principal values and its relation to O(2p) hybridization with the B-atom d-states is analyzed in Sec. IV A.

Table II compares the results for  $\text{SrTiO}_3$  and  $\text{BaTiO}_3$  in Table I with recent single crystal measurements<sup>54</sup> and with earlier powder spectrum measurements of the isotropic shifts. Isotropic and uniaxial components of the chemical shift tensors are given, where  $\delta_{\text{ax}} = (\delta_z - \delta_{\text{iso}})/2$ , using Eq. (2). In  $\text{SrTiO}_3$ , the calculated  $\delta_{\text{iso}}$  and  $\delta_{\text{ax}}$  differ from experiment by  $\simeq 20$  ppm and  $\simeq 9$  ppm respectively. In  $\text{BaTiO}_3$ ,  $\delta_{\text{iso}}$  calculated and experiment values differ by at most 16 ppm.

Table III compares the results for  $\text{PbTiO}_3$  and  $\text{PbZrO}_3$  isotropic shifts  $\delta_{\text{iso}}$  (derived from Table I) with well resolved measured powder spectra.<sup>55</sup> For both systems, the calculated results differ from experiment by no more than

21 ppm, with an average discrepancy of approximately 10 ppm. Differences of relative shifts between chemical sites are smaller in most cases. For example, in tetragonal  $\text{PbTiO}_3$  the calculated B3LYP splitting between the two inequivalent O sites is  $\simeq 200$  ppm, in good agreement with measured powder spectra.<sup>55</sup>

#### IV. DISCUSSION

A key feature in the electronic structure of transition metal perovskites are the covalent interactions between the O(2p) and the (formally) unoccupied transition metal-d states. Indeed, the delicate balance between covalent and electrostatic ionic interactions is responsible for the wide variety of interesting properties exhibited by these materials and related alloys. In this section, we analyze the calculated chemical shieldings in Sec. III in relation to p-d hybridization.

The measured NMR  $^{17}\text{O}$  spectra show narrow well separated peaks in these materials, indicating that second-order quadrupolar broadening and, thus, the electric field gradients (EFGs) are small,<sup>55</sup> consistent with first principles calculations of O EFGs.<sup>53,56</sup> For the systems studied here, all the O sites are clearly resolved in the measurements, and the chemical shielding tensor largely determines the second order quadrupolar peak positions.<sup>55</sup>

##### A. p-d hybridization and anisotropy of oxygen chemical shielding

As mentioned, a striking feature in Table I is the large anisotropy of the chemical shielding principal values. This is due to hybridization between the O(2p) and virtual B-site d-states. The qualitative features can be understood from a simplified picture, which focuses on the B-O-B quasilinear structural unit (Fig. 1). In a linear molecule, the dependence of  $\hat{\sigma}$  on the direction of the applied field  $\mathbf{B}_{\text{ext}}$  is particularly simple, if we choose to locate the vector potential gauge origin at the target nucleus.<sup>57,58</sup> In this case, when  $\mathbf{B}_{\text{ext}}$  is parallel to the molecular axis, only the diamagnetic (shielding) component contributes to  $\hat{\sigma}$ ; when  $\mathbf{B}_{\text{ext}}$  is perpendicular to the axis, both diamagnetic and paramagnetic (deshielding) components contribute. (Note that the calculated  $\hat{\sigma}$  are invariant under a change of the gauge origin. Consequently, we are free to interpret the  $\hat{\sigma}$  values as if they had been calculated with any particular choice of origin.) The diamagnetic component depends only on ground state wave functions, while the paramagnetic component depends on virtual transitions to unoccupied states, *i.e.*, occupation of virtual states in the first order perturbed wave functions. In a DFT or HF calculation, this implies that large paramagnetic contributions could be expected, if there are low lying unoccupied one particle eigenstates that are strongly coupled to occupied states. This is the case in these materials, where there is strong coupling

between O(2p) and virtual B-site d-states.

In cubic  $\text{SrTiO}_3$ , for example, when  $\mathbf{B}_{\text{ext}}$  is applied along the Ti-O bond direction ( $z$ -direction), the O nucleus is shielded by the applied field (*i.e.*, the principal value  $\sigma_z = 90$  is positive [Eq. (1)]). By contrast, when  $\mathbf{B}_{\text{ext}}$  is perpendicular to the Ti-O bond, the O nucleus is strongly deshielded ( $\sigma_x = \sigma_y = -343$ ) as shown in Table I. According to this B-O-B picture, we would infer that only diamagnetic contributions should contribute to  $\sigma_z = 90$ , and the positive  $\sigma_z = 90$  value is consistent with this. Similarly, we would attribute the deshielded  $\sigma_x = \sigma_y = -343$  value to paramagnetic contributions arising from the O(2p)-Ti(3d) hybridization mechanism. This interpretation is supported by the fake  $\text{SrTiO}_3$  calculations, where removal of Ti d basis functions quenches O(2p)-Ti(3d) hybridization and results in nearly isotropic principal value components,  $\sigma_x = \sigma_y \simeq \sigma_z$ .

While qualitatively correct, the simple B-O-B model leaves out important crystalline effects. Thus the  $\text{SrTiO}_3$  GIAO total shielding value  $\sigma_z = 116$  arises from cancellation of large diamagnetic  $\sigma_{d,z} = 371$  and smaller paramagnetic  $\sigma_{p,z} = -255$  components. Note that the fake  $\sigma_{p,z} = -262$  value is similar to the normal  $\sigma_{p,z} = -255$  value; in addition  $\sigma_{p,xy} \simeq \sigma_{p,z}$  in the fake calculation. We therefore attribute the presence of a non-zero  $\sigma_{p,z}$  to interactions with other atoms in the crystal, which are neglected in the simple B-O-B picture.

Variations in B-O-B bond distances will affect O(2p)-B( $nd$ ) hybridization, and this should be reflected by corresponding changes in the calculated oxygen chemical shieldings. This is the case, as seen in Figure 2, which shows that the isotropic  $\delta_{\text{iso}}$  and uniaxial  $\delta_{\text{ax}}$  chemical shifts [Eq. (2)] exhibit a remarkably linear variation as a function of  $r_s$ , the shortest B-O bond length of the targeted O atom.<sup>59</sup> Indeed,  $\delta_{\text{iso}}$  changes by more than a factor of two over the plotted range.

The linear behavior is largely due to the deshielding  $\sigma_x$  and  $\sigma_y$  components in Table I. To frame the discussion in terms of the paramagnetic components of the shielding tensors, we first subtract the diamagnetic component of the isolated  $\text{O}^{2-}$  atom,  $\sigma(\text{O}^{2-}) = 410$  ppm, defining  $\sigma_{p,z} = \sigma_z - \sigma(\text{O}^{2-})$  and  $\sigma_{p,xy} = (\sigma_x + \sigma_y)/2 - \sigma(\text{O}^{2-})$ . These are plotted in Fig. 3. An alternative choice would be to plot the GIAO paramagnetic component. Even had we done GIAO calculations for all the different O-sites, this choice is not necessarily better, since both the diamagnetic and paramagnetic GIAO components include contributions from neighboring atoms.<sup>44</sup> Moreover, the separation into diamagnetic and paramagnetic components is, at best, only qualitatively useful, since the separate components depend on the choice of gauge method. The present choice is physically motivated, using a well defined diamagnetic reference system. As indicated by the  $\text{SrTiO}_3$  GIAO diamagnetic components, which differ by only  $\simeq 40 - 50$  ppm from the  $\text{O}^{2-}$  value (Table I), this subtraction largely removes the closed shell diamagnetic response. In any case, our definition of  $\sigma_p$  simply shifts

all  $\sigma$  principal values by a constant. As seen in Fig. 3, both  $\sigma_{p,z}$  and  $\sigma_{p,xy}$  vary linearly with  $r_s$ . The average slope of  $\sigma_{p,xy}$  is  $\simeq 5$  times larger in magnitude than that of  $\sigma_{p,z}$ . This shows that the linear behavior in Fig. 2 is largely due to the variations of the deshielding  $\sigma_x$  and  $\sigma_y$  components, which arise from the p-d hybridization mechanism.

The p-d hybridization mechanism also plays a key role in producing the anomalously large dynamical (Born) effective charge tensors  $Z^*$ , which are universally seen in perovskite ferroelectrics for the O, transition metal B, and Pb atoms.<sup>60,61,62,63,64</sup> In cubic BaTiO<sub>3</sub>, SrTiO<sub>3</sub>, PbTiO<sub>3</sub> and PbZrO<sub>3</sub>,  $Z_{zz}^*(O)$  (the component along the Ti-O bond) takes on the values  $-5.59$ ,  $-5.66$ ,  $-5.83$ , and  $-4.81$ <sup>60</sup>, respectively, which is much larger than the nominal  $-2$  value for O<sup>2-</sup>. By contrast, the perpendicular components  $Z_{xx}^*(O)=Z_{yy}^*(O)$  are given by  $-2.11$ ,  $-2.00$ ,  $-2.56$ ,  $-2.48$ , respectively, which are much closer to the nominal value, since these stretch the B-O bond only in second order. Similarly, all  $Z^*(B^{4+}) \simeq 6 - 7$  are anomalously large, since these involve the flow of dynamic charge as the B-O bond is stretched or compressed. [In PbTiO<sub>3</sub> and PbZrO<sub>3</sub>,  $Z^*(Pb) \simeq 4$  is anomalously large compared to  $Z^*(Ba) \simeq Z^*(Sr) \simeq 2.6$ , due to strong Pb-O covalency, and this is reflected in the somewhat more anomalous  $Z_{xx}^*(O)$  and  $Z_{yy}^*(O)$  in the Pb based crystals.] Artificially decreasing the p-d hybridization, as in Ref. 65, resulted in nominal values of all the  $Z^*$ .

Similarly, the fake SrTiO<sub>3</sub> calculation eliminates B(d)-O(2p) paramagnetic contributions to  $\hat{\sigma}$  and largely removes the anisotropy between  $\sigma_x \simeq \sigma_y$  and  $\sigma_z$  components. B(d)-O(2p) covalency is essential for ferroelectricity in transition metal perovskites, mitigating the repulsion between otherwise rigid ion-cores, which tends to suppress ferroelectric distortion; under pressure, this mechanism eventually fails and ferroelectricity disappears.<sup>66</sup> Figure 3 shows that the the anisotropy between  $\sigma_{p,xy}$  and  $\sigma_{p,z}$  increases linearly with decreasing  $r_s$ , consistent with this picture, and indicating a strengthening of the p-d hybridization mechanism as  $r_s$  is reduced.

### B. Exchange and correlation effects

Despite the fact that the B3LYP band gap is nearly a factor of two larger than that of GGA, the results in Tables I and II are fairly similar, with the exception of PbTiO<sub>3</sub>, where the B3LYP results are in better agreement with experiment (Table III; Sec. IV C). Although larger band gaps result in larger energy denominators in the paramagnetic perturbative equations,<sup>57,58</sup> there is little difference in the shieldings between the two methods. Similarly, a significant deshielded SrTiO<sub>3</sub> RHF paramagnetic component is evident in Table I, despite the much larger RHF HOMO-LUMO gap of 8.8 eV, compared to the B3LYP 3.6 eV gap. The apparent dependence of the chemical shielding on the band gap can be somewhat misleading, however, since the transverse paramag-

netic component of the first order current density could be made to vanish under suitable gauge transformations within the CSGT gauge method.<sup>42,67</sup> The entire shielding would then be given by the diamagnetic component, which depends only on the occupied single particle states. Similar observations were made regarding calculations of the the spontaneous polarization  $P$  and  $Z^*$  in ferroelectric perovskites, where RHF results for these quantities were found to be in good numerical agreement with both experiment and with DFT calculations,<sup>68,69</sup> both methods yielding anomalously large  $Z^*$ .

### C. Comparison of oxygen chemical shifts with experiment

The calculated results in Table II for SrTiO<sub>3</sub> and BaTiO<sub>3</sub> are in very good agreement with single crystal measurements. Overall, both B3LYP and GGA yield similar agreement with experiment, while RHF is significantly worse. Comparisons for the cubic and ferroelectric P4mm tetragonal BaTiO<sub>3</sub> phases should keep in mind evidence for static and/or motional disorder of local structures suggested by experiment<sup>54,70,71</sup> and theory,<sup>72,73</sup> since the present calculations were performed for ordered crystalline structures.

In PbTiO<sub>3</sub>, the O<sub>ax</sub> atom has two nn Ti atoms along the polar direction, with one short 1.77 Å and one long 2.39 Å bond length, while the O<sub>eq</sub> has two equal bonds of 1.98 Å. The experimental assignment of the two measured peaks is simplified by the fact that the relative integrated intensities of the two O spectral peaks corresponds to the 1:2 ratio of the O<sub>eq</sub> to O<sub>ax</sub> atoms in the simple 5-atom primitive unit cell.<sup>55</sup> The large  $\simeq 200$  ppm experimentally observed<sup>55</sup> splitting between the O<sub>ax</sub> and O<sub>eq</sub> reflects their very different Ti-O bond lengths. The B3LYP calculated chemical shifts in Table III reproduce the  $\simeq 200$  ppm splitting, while GGA underestimates it by  $\simeq 50$  ppm. Basis set and cluster size convergence errors (Section II C) can be expected to largely cancel in these calculated splittings, reducing the residual uncertainty to less than about 10 ppm. We are not aware of any measurements of the <sup>17</sup>O uniaxial asymmetry in PbTiO<sub>3</sub>.

In PbZrO<sub>3</sub> the peak assignments are more difficult, because four of the five inequivalent oxygen sites have the same ratio of occurrence in the unit cell. In Ref. 55 the peak assignment in the NMR spectrum was made based on the assumptions that (1) the proximity of the Zr cation plays the most important shielding role and (2) that the largest chemical shift corresponds to the largest bond length. The present calculations indicate that the first assumption is correct, but not the second. Instead, as seen in Fig. 2, the largest chemical shift corresponds to shortest bond distance between the targeted O atom and its nearest B atom. Indeed, the figure shows that this holds true, not only for PbZrO<sub>3</sub>, but across several compounds, over a wide range of chemical shifts. Our

calculations indicate that chemical shift site assignments for the O(4) and O(5) atoms in Ref. 55 (their Table 1) should be reversed. Finally, we note that differences between theory and experiment in the relative splittings are smaller than those of the absolute splittings, *i.e.*, a rigid shift of the calculated B3LYP (GGA) values in Table III by  $\simeq 10$  ppm ( $\simeq -15$  ppm) removes most of the the discrepancies.

## V. SUMMARY

We have shown that first-principles embedded cluster calculations, using the DFT hybrid B3LYP method, can accurately calculate O chemical shifts for prototypical perovskite structure transition metal oxides. Calculated isotropic and uniaxial chemical shifts were found to be in good agreement with recent single crystal NMR  $^{17}\text{O}$  measurements for  $\text{SrTiO}_3$  and  $\text{BaTiO}_3$ . For ferroelectric P4mm  $\text{BaTiO}_3$  and  $\text{PbTiO}_3$ , the calculations accurately reproduced measured power spectra NMR isotropic chemical shifts  $\delta_{\text{iso}}$  for the two inequivalent O sites. The large  $\simeq 200$  ppm experimental splitting in P4mm  $\text{PbTiO}_3$  is well reproduced by B3LYP, but DFT/GGA underestimates it by  $\simeq 50$  ppm. In  $\text{PbZrO}_3$ , experimental and calculated  $\delta_{\text{iso}}$  are in very good agreement, but experimental peak assignments are more difficult, since four of the five inequivalent O sites appear in the same ratio. Our calculations, indicate a correction of the experimental assignments in Ref. 55.

Our most notable findings are 1) a large anisotropy in

the chemical shielding tensor, between deshielded  $\sigma_x \simeq \sigma_y$  and shielded  $\sigma_z$  components, the latter principal axis being along the Ti-O bond, and 2) a nearly linear variation, across all the systems studied, of  $\delta_{\text{iso}}$  and  $\delta_{\text{ax}}$  as a function of B-O-B bond asymmetry. We have shown that the anisotropy and linear variation arise from large paramagnetic contributions to  $\sigma_x$  and  $\sigma_y$  due to virtual transitions between O(2p) and unoccupied B(nd) states. A qualitative explanation of the anisotropy was given and then confirmed by calculations for a fake material with no d-states.

We have shown that O NMR chemical shifts are a sensitive indicator of the local structure in perovskites with transition metal B-site atoms, due to covalent O(2p)-B(nd) interactions. This indicates that  $^{17}\text{O}$  NMR spectroscopy, coupled with first principles calculations, can be an especially useful tool to study the local structure in complex perovskite alloys.

## VI. ACKNOWLEDGMENTS

This work was supported by ONR grants N00014-08-1-1235 and N00014-09-1-0300. DLP acknowledges support from a Virginia Space Grant Consortium Graduate Research Fellowship. Calculations were performed at the National Energy Research Scientific Computing Center (NERSC) and the Center for Piezoelectric by Design. We acknowledge useful discussions with Gina Hoatson and Robert L. Vold.

- 
- <sup>1</sup> J. Scott, *Science* **315**, 954 (2007).
- <sup>2</sup> K. M. Rabe, C. H. Ahn, , and J.-M. Triscone, eds., *Physics of Ferroelectrics: A Modern Perspective* (Springer, Berlin, 2007).
- <sup>3</sup> D. H. Zhou, G. L. Hoatson, R. L. Vold, and F. Fayon, *Phys. Rev. B* **69**, 134104 (2004).
- <sup>4</sup> D. H. Zhou, G. L. Hoatson, and R. L. Vold, *J. Magn. Reson.* **167**, 242 (2004).
- <sup>5</sup> M. Vijayakumar, G. L. Hoatson, and R. L. Vold, *Phys. Rev. B* **75**, 104104 (2007).
- <sup>6</sup> M. H. Cohen and F. Reif, *Sol. St. Phys.* **5**, 321 (1957).
- <sup>7</sup> T. Helgaker, M. Jaszunski, and K. Ruud, *Chem. Rev.* **99**, 293 (1999), ISSN 0009-2665.
- <sup>8</sup> G. Valerio, A. Goursot, R. Vetrivel, O. Malkina, V. Malkin, and D. R. Salahub, *J. Am. Chem. Soc.* **120**, 11426 (1998).
- <sup>9</sup> G. Valerio and A. Goursot, *J. Phys. Chem. B* **103**, 51 (1999).
- <sup>10</sup> J. A. Tossel, *Chem. Phys. Lett.* **303**, 435 (1999).
- <sup>11</sup> J. A. Tossel, *Phys. Chem. Minerals* **27**, 70 (1999).
- <sup>12</sup> D. Stueber, F. N. Guenneau, and D. M. Grant, *J. Chem. Phys.* **114**, 9236 (2001).
- <sup>13</sup> D. Stueber, *Concepts Magn Reson* **28A**, 347 (2006).
- <sup>14</sup> F. Mauri, B. G. Pfommer, and S. G. Louie, *Phys. Rev. Lett.* **77**, 5300 (1996).
- <sup>15</sup> C. J. Pickard and F. Mauri, *Phys. Rev. B* **63**, 245101 (2001).
- <sup>16</sup> M. Profeta, F. Mauri, and C. J. Pickard, *J. Am. Chem. Soc.* **125**, 541 (2003).
- <sup>17</sup> T. Thonhauser, D. Ceresoli, D. Vanderbilt, and R. Resta, *Phys. Rev. Lett.* **95**, 137205 (2005).
- <sup>18</sup> J. Shi, G. Vignale, D. Xiao, and Q. Niu, *Phys. Rev. Lett.* **99**, 197202 (2007).
- <sup>19</sup> T. Thonhauser, D. Ceresoli, A. A. Mostofi, R. Resta, and D. Vanderbilt, preprint: arXiv:0709.4429v2.
- <sup>20</sup> D. Ceresoli, U. Gerstmann, A. P. Seitsonen, and F. Mauri, preprint: arXiv:0904.1988v1.
- <sup>21</sup> R. L. Martin, *Phys. Rev. Lett.* **75**, 744 (1995).
- <sup>22</sup> R. L. Martin and P. J. Hay, *J. Chem. Phys.* **98**, 8680 (1993).
- <sup>23</sup> P. Husser, H. U. Suter, E. P. Stoll, and P. F. Meier, *Phys. Rev. B* **61**, 1567 (2000).
- <sup>24</sup> S. Renold, S. Plibersek, E. P. Stoll, T. Claxton, and P. F. Meier, *Eur. Phys. J. B* **23**, 3 (2001).
- <sup>25</sup> M. J. Frisch, G. W. T. H. B. Schlegel, G. E. Scuseria, M. A. Robb, J. R. Cheeseman, V. G. Zakrzewski, J. A. Montgomery, Jr., R. E. Stratmann, J. C. Burant, et al., *Gaussian 98, Revision A.11.4*, Gaussian, Inc., Pittsburgh PA, 2002.
- <sup>26</sup> M. J. Frisch, G. W. Trucks, H. B. Schlegel, G. E. Scuseria, M. A. Robb, J. R. Cheeseman, J. A. Montgomery, Jr.,

- T. Vreven, K. N. Kudin, J. C. Burant, et al., *Gaussian 03, Revision C.02*, Gaussian, Inc., Wallingford, CT, 2004.
- <sup>27</sup> K. L. Schuchardt, B. T. Didier, T. Elsethagen, L. Sun, V. Gurumoorathi, J. Chase, J. Li, and T. L. Windus, *J. Chem. Inf. Model.* **47**, 1045 (2007).
- <sup>28</sup> M. Kaupp, M. Bühl, and V. Malkin, *Calculation of NMR and EPR Parameters: Theory and Applications* (Wiley-VCH, 2004).
- <sup>29</sup> J. Vaara, *Phys. Chem. Chem. Phys.* **9**, 5399 (2007).
- <sup>30</sup> M. K. Klintonberg, S. E. Derenzo, and M. J. Weber, *Comput. Phys. Commun.* **131**, 120 (2000).
- <sup>31</sup> S.-E. Park and T. R. Shrout, *J. Appl. Phys.* **82**, 1804 (1997).
- <sup>32</sup> A. D. Buckingham, *Mol. Phys.* **22**, 1127 (1971).
- <sup>33</sup> R. F. Schneider, *J. Chem. Phys.* **48**, 4905 (1968).
- <sup>34</sup> F. Anet and D. J. O'Leary, *Concepts in Magn. Reson* **3**, 193 (1991).
- <sup>35</sup> F. Anet and D. J. O'Leary, *Concepts in Magn. Reson* **4**, 35 (1992).
- <sup>36</sup> J. F. Baugher, P. C. Taylor, T. Oja, and P. J. Bray, *The Journal of Chemical Physics* **50**, 4914 (1969).
- <sup>37</sup> R. G. Gordon and Y. S. Kim, *The Journal of Chemical Physics* **56**, 3122 (1972).
- <sup>38</sup> M. J. Mehl, R. J. Hemley, and L. L. Boyer, *Phys. Rev. B* **33**, 8685 (1986).
- <sup>39</sup> R. E. Cohen, L. L. Boyer, and M. J. Mehl, *Phys. Rev. B* **35**, 5749 (1987).
- <sup>40</sup> N. W. Winter, R. M. Pitzer, and D. K. Temple, *J. Chem. Phys.* **86**, 3549 (1987).
- <sup>41</sup> D. Singh, *Planewaves, Pseudopotentials, and the LAPW Method* (Kluwer Academic Publishers, 1994).
- <sup>42</sup> T. A. Keith and R. F. W. Bader, *Chem. Phys. Lett.* **210**, 223 (1993).
- <sup>43</sup> J. R. Cheeseman, G. W. Trucks, T. A. Keith, and M. J. Frisch, *J. Chem. Phys.* **104**, 5497 (1996).
- <sup>44</sup> R. Ditchfield, *Mol. Phys.* **27**, 789 (1974).
- <sup>45</sup> R. K. Harris, E. D. Becker, S. M. C. D. Menezes, P. Granger, R. E. Hoffman, and K. W. Zilm, *Solid State Nucl. Magn. Reson* **33**, 41 (2008).
- <sup>46</sup> The isotropic component should average out to zero when the measurement is performed under magic angle spinning (MAS). MAS measurements were made for most materials except for some of the SrTiO<sub>3</sub> and BaTiO<sub>3</sub>. For cases when the sample is oriented at an angle other than the magic angle the magnetic susceptibility of the material will change the oxygen chemical shift by no more than 3 ppm if we assume that the samples are homogenous and in an infinite cylinder. See Ref. 45 for more information.
- <sup>47</sup> A. D. Becke, *J. Chem. Phys.* **98**, 5648 (1993).
- <sup>48</sup> K. Burke, J. P. Perdew, and Y. Wang, *Electronic Density Functional Theory: Recent Progress and New Directions* (Plenum, 1998).
- <sup>49</sup> O. Madelung, U. Rossler, and M. Schulz, eds., *Landolt-Börnstein - Group III Condensed Matter*, vol. 41E (Springer-Verlag, 2000).
- <sup>50</sup> G. H. Kwei, A. C. Lawson, and S. J. L. Billinge, *J. Phys. Chem.* **97**, 2368 (1993).
- <sup>51</sup> W. Schildkamp and K. Fischer, *Z. Kristallogr.* **155**, 217 (1981).
- <sup>52</sup> R. Nelmes and W. Kuhs, *Solid State Commun.* **54**, 721 (1985).
- <sup>53</sup> M. D. Johannes and D. J. Singh, *Phys. Rev. B* **71**, 212101 (2005).
- <sup>54</sup> R. Blinc, V. V. Laguta, B. Zalar, M. Itoh, and H. Krakauer, *J. Phys.: Condens. Matter* **20**, 085204 (2008).
- <sup>55</sup> A. Baldwin, P. A. Thomas, and R. Dupree, *J. Phys.: Condens. Matter* **17**, 7159 (2005).
- <sup>56</sup> D. Mao, E. J. Walter, H. Krakauer, and Z. Wu, *Phys. Rev. B* **76**, 014105 (2007).
- <sup>57</sup> N. F. Ramsey, *Phys. Rev.* **78**, 699 (1950).
- <sup>58</sup> N. F. Ramsey, *Phys. Rev.* **83**, 540 (1951).
- <sup>59</sup> The short B-O bond length  $r_s$  can be expressed as  $r_s = r_{\text{avg}} - \Delta/2$ , where  $r_{\text{avg}}$  is the average of the short and long B-O distances and  $\Delta$  describes the asymmetry of the B-O-B chain. Since  $r_{\text{avg}} \simeq 2 \text{ \AA}$  across these systems,  $r_s$  is also a measure of the dimerization or bond length asymmetry of the B-O-B chain.
- <sup>60</sup> W. Zhong, R. D. King-Smith, and D. Vanderbilt, *Phys. Rev. Lett.* **72**, 3618 (1994).
- <sup>61</sup> R. D. King-Smith and D. Vanderbilt, *Phys. Rev. B* **47**, 1651 (1993).
- <sup>62</sup> R. Resta, *Rev. Mod. Phys.* **66**, 899 (1994).
- <sup>63</sup> C.-Z. Wang, R. Yu, and H. Krakauer, *Phys. Rev. B* **54**, 11161 (1996).
- <sup>64</sup> P. Ghosez, J.-P. Michenaud, and X. Gonze, *Phys. Rev. B* **58**, 6224 (1998).
- <sup>65</sup> M. Posternak, R. Resta, and A. Baldereschi, *Phys. Rev. B* **50**, 8911 (1994).
- <sup>66</sup> R. E. Cohen and H. Krakauer, *Phys. Rev. B* **42**, 6416 (1990).
- <sup>67</sup> R. Zanasi, P. Lazzeretti, M. Malagoli, and F. Piccinini, *The Journal of Chemical Physics* **102**, 7150 (1995), URL <http://link.aip.org/link/?JCP/102/7150/1>.
- <sup>68</sup> S. Dall'Olio, R. Dovesi, and R. Resta, *Phys. Rev. B* **56**, 10105 (1997).
- <sup>69</sup> L. Fu, E. Yaschenko, L. Resca, and R. Resta, *Phys. Rev. B* **57**, 6967 (1998).
- <sup>70</sup> R. Comes, M. Lambert, and A. Guinier, *Solid State Commun.* **6**, 715 (1968).
- <sup>71</sup> E. A. Stern and Y. Yacoby, *J. Phys. Chem. Solids* **57**, 1449 (1996), proceeding of the 3rd Williamsburg Workshop on Fundamental Experiments on Ferroelectrics.
- <sup>72</sup> R. Yu and H. Krakauer, *Phys. Rev. Lett.* **74** (1995).
- <sup>73</sup> H. Krakauer, R. Yu, C. Z. Wang, K. M. Rabe, and U. V. Waghmare, *J. Phys.: Condens. Matter* **11**, 3779 (1999).
- <sup>74</sup> R. E. Wasylshen and D. Bryce, *J. Chem. Phys.* **117**, 10061 (2002).
- <sup>75</sup> T. J. Bastow, P. J. Dirken, and M. E. Smith, *J. Phys. Chem.* **100**, 18539 (1996).
- <sup>76</sup> D. R. Spearings and J. Stebbins, *J. Am. Ceram. Soc* **77**, 3263 (1994).
- <sup>77</sup> V. Anuradha, Master's thesis, University of Warwick, UK (1990).



TABLE I: Calculated oxygen chemical shielding principal values (in ppm) for SrTiO<sub>3</sub>, BaTiO<sub>3</sub>, PbTiO<sub>3</sub> and PbZrO<sub>3</sub>. In all cases, “z” denotes the principal axis that is most closely along the B-O bond direction. Unless otherwise indicated, the CSGT gauge method was used, with B3LYP for exchange and correlation. For some cases, GGA results are given in parenthesis. RHF and GIAO gauge method B3LYP results are given for SrTiO<sub>3</sub>. GIAO results for the isolated diamagnetic O<sup>2-</sup> atom are also shown. See the text for a discussion of the fake SrTiO<sub>3</sub> calculation. For PbZrO<sub>3</sub>, we adopt the site labeling convention of Ref. 53; the O(i) site notation of Ref. 55 is also given in brackets.

	$\sigma_x$	$\sigma_y$	$\sigma_z$
SrTiO <sub>3</sub> (cubic)			
	-343 (-353)	-343 (-353)	90 ( 46)
GIAO diamag.	347	347	371
GIAO paramag.	-694	-694	-255
GIAO total	-347	-347	116
RHF	-134	-134	201
O <sup>2-</sup>	410	410	410
fake calculation			
GIAO diamag.	397	397	448
GIAO paramag.	-228	-228	-262
GIAO total	169	169	186
BaTiO <sub>3</sub>			
cubic	-413 (-414)	-413 (-414)	97 (49)
P4mm	O <sub>ax</sub> -505 (-480)	-505 (-480)	116 (70)
	O <sub>eq</sub> -401 (-407)	-353 (-355)	87 (40)
R3m	-423 (-416)	-412 (-406)	97 (51)
PbTiO <sub>3</sub> (P4mm)			
	O <sub>ax</sub> -608 (-562)	-608 (-562)	163 (123)
	O <sub>eq</sub> -263 (-286)	-219 (-228)	13 (-32)
PbZrO <sub>3</sub> (Pbam)			
O1-4g [O(1)]	-172 (-197)	-107 (-130)	85 ( 48)
O1'-4g [O(2)]	-132 (-158)	-104 (-126)	77 ( 40)
O2-8i [O(3)]	-147 (-171)	-139 (-162)	100 ( 64)
O3-4f [O(4)] <sup>a</sup>	-93 (-118)	-64 ( -90)	62 ( 26)
O4-4e [O(5)]	-251 (-269)	-223 (-239)	175 (136)

<sup>a</sup>Note: our calculations suggest that the assignment of the O3-4f[O(4)] and O4-4e[O(5)] peaks should be reversed in Ref. 55, as done here.

TABLE II: Comparison between calculated and measured single crystal and powder spectra  $^{17}\text{O}$  chemical shifts (in ppm) for  $\text{BaTiO}_3$  and  $\text{SrTiO}_3$ . Calculated isotropic shifts  $\delta_{\text{iso}}$  and uniaxial components  $\delta_{\text{ax}}$  are derived from Table I, referenced to liquid water,  $\sigma_{\text{iso}}^{\text{water}} = 287.5$  ppm (Ref. 74). Calculated values are from B3LYP (GGA values are in parenthesis), and RHF results are also shown for  $\text{SrTiO}_3$ .

		$\delta_{\text{iso}}$		$\delta_{\text{ax}}$	
		Theory	Expt.	Theory	Expt.
<b>SrTiO<sub>3</sub></b>					
cubic		486 (507)	$467 \pm 5^a, 465^b$	-144 (-132)	$-135.3 \pm 5^a$
cubic RHF		310		-112	
<b>BaTiO<sub>3</sub></b>					
cubic		530 (547)	$546 \pm 5^a$	-170 (-154)	$-150 \pm 1^a$
P4mm	O <sub>ax</sub>	585 (584)	$570 \pm 5^a, 553^c, 564^d$	-207 (-183)	$-171 \pm 1^a$
	O <sub>eq</sub>	510 (528)	$520 \pm 5^a, 530^c, 523^d$	-155 (-140)	$-142 \pm 1^a$

<sup>a</sup>Single crystal experimental values are from Ref. 54

<sup>b</sup>Powder results Ref. 75

<sup>c</sup>Powder results Ref. 76

<sup>d</sup>Powder results Ref. 77

TABLE III: Comparison between calculated and experimental isotropic chemical shifts  $\delta_{\text{iso}}$  (in ppm) for  $\text{PbTiO}_3$  and  $\text{PbZrO}_3$ . Calculated isotropic shifts are derived from Table I, referenced to liquid water,  $\sigma_{\text{iso}}^{\text{water}} = 287.5$  ppm (Ref. 74). Calculated values are from B3LYP (GGA values are in parenthesis). For  $\text{PbZrO}_3$ , we adopt the site labeling convention of Ref. 53; the O(i) site notation of Ref. 55 is also given.

	Theory	Expt. <sup>a</sup>
<b>PbTiO<sub>3</sub></b>		
O <sub>ax</sub>	639 (621)	$647 \pm 2$
O <sub>eq</sub>	444 (469)	$443 \pm 2$
<b>PbZrO<sub>3</sub></b>		
O1-4g [O(1)]	352 (380)	$365 \pm 2$
O1'-4g [O(2)]	340 (369)	$351 \pm 2$
O2-8i [O(3)]	349 (377)	$356 \pm 2$
O3-4f [O(4)] <sup>b</sup>	319 (348)	$329 \pm 2$
O4-4e [O(5)]	387 (412)	$408 \pm 2$

<sup>a</sup>Experimental values are from Ref. 55

<sup>b</sup>Note: our calculations suggest that the assignment of the O3-4f[O(4)] and O4-4e[O(5)] peaks should be reversed in Ref. 55, as done here.

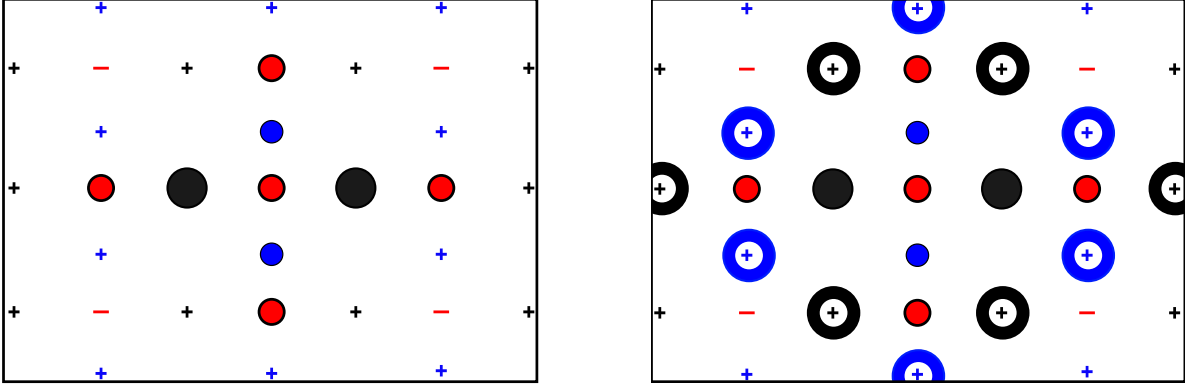


FIG. 1: Illustration of cluster embedding for the O-centered  $A_4B_2O_{15}$  quantum atom (QM) cluster (Sec. II B 1), shown for a [110] plane of the ideal perovskite structure. The QM A, B, and O atoms are depicted by filled black, blue and red circles, respectively. In the left panel, the QM atoms are embedded in point charges, “+” or “-” signs colored coded according to the QM atom they replace in the crystalline lattice. In the right panel, the boundary O QM atoms have had their nearest and next-nearest neighbor cation point charges replaced by “empty” pseudopotentials (Sec. II B 3), indicated by thick large circles, with corresponding color coding.

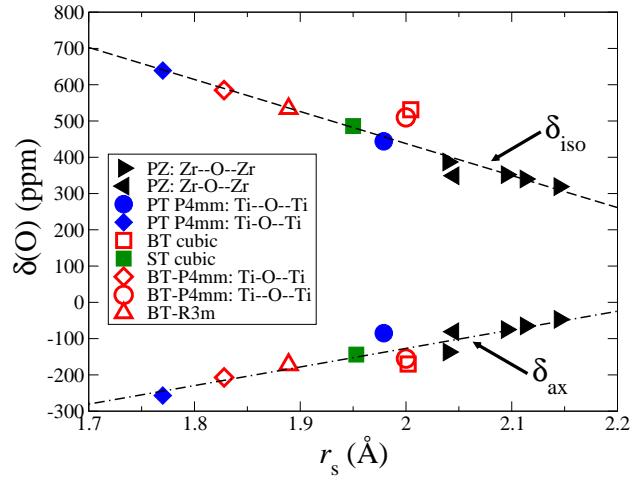


FIG. 2: Calculated oxygen isotropic  $\delta_{\text{iso}}$  and uniaxial  $\delta_{\text{ax}}$  chemical shifts in  $\text{SrTiO}_3$  (ST),  $\text{BaTiO}_3$  (BT),  $\text{PbTiO}_3$  (PT),  $\text{PbZrO}_3$  (PZ), as a function of  $r_s$ , the shortest B-O bond length of the targeted O atom. The notation B--O--B indicates O atoms with two equidistant nn B atoms, and B-O--B indicates an O atom with one short and one long nn B bond (*e.g.*, along the polar *c*-axis in P4mm  $\text{PbTiO}_3$ ). The straight lines are linear fits.

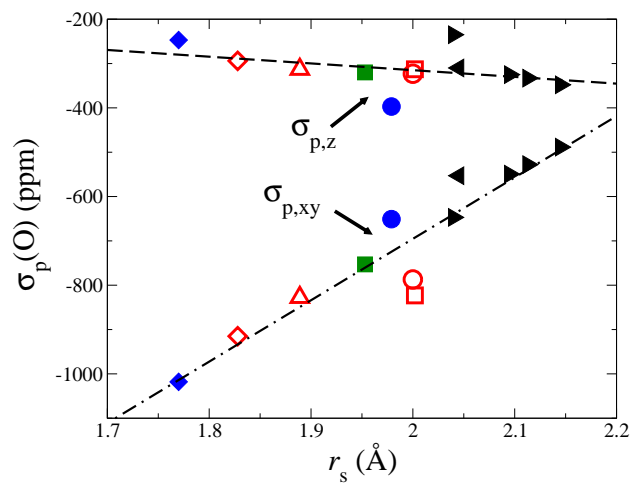


FIG. 3: Calculated paramagnetic  $\sigma_{p,z}$  and  $\sigma_{p,xy}$  components (see text), as a function of  $r_s$ , the shortest B-O bond length of the targeted O atom. The straight lines are linear regressions of the points. Symbols as in Fig. 2.